metals

Article

Comparison of Fluid Flow and Temperature Distribution in a Single-Strand Tundish with Different Flow Control Devices

Dong-Yuan Sheng [1,2,*] and Dengfu Chen [3]

[1] Department of Materials Science and Engineering, Royal Institute of Technology, 10044 Stockholm, Sweden
[2] Westinghouse Electric Sweden AB, 72163 Västerås, Sweden
[3] Laboratory of Metallurgy and Materials, College of Materials Science and Engineering, Chongqing University, Chongqing 400044, China; chendfu@cqu.edu.cn
* Correspondence: shengdy@kth.se; Tel.: +46-8790-8467

Abstract: The effects of flow control devices (FCD) in a single-strand tundish, including weir, dam, turbulence inhibitor and gas curtain, have been investigated using water model experiments and CFD simulations. A scaled-down water model was built up to visualize flow pattern and measure the residence-time distribution (RTD) of different tundish configurations. A CFD model was applied to calculate the fluid flow, heat transfer and RTD curves in the prototype tundish under the nonisothermal conditions. The Eulerian–Lagrangian approach was applied to investigate the bubble flow in the system. The results show that each FCD has its own unique function to control the flow. It is important to evaluate the combined effects of FCD based on their installations. The molten steel flow in the tundish could be improved if these flow control devices were arranged properly.

Keywords: flow control device (FCD); heat transfer; computational fluid dynamics (CFD); residence-time distribution (RTD); multiphase flow

check for updates

Citation: Sheng, D.-Y.; Chen, D. Comparison of Fluid Flow and Temperature Distribution in a Single-Strand Tundish with Different Flow Control Devices. *Metals* **2021**, *11*, 796. https://doi.org/10.3390/met11050796

Academic Editor: Markéta Tkadlečková

Received: 25 April 2021
Accepted: 13 May 2021
Published: 14 May 2021

1. Introduction

Considerable research efforts have been made over many decades to fully exploit the metallurgical performance of tundish [1–4]. The work on optimizing the flow pattern in the tundish to meet the demand of improvement in steel quality is an important research topic for metallurgists. A modern tundish is designed to provide maximum opportunity for the control of fluid flow, heat transfer and inclusion removal. Tundish design varies widely owing to the differences in the end products, number of strands, and operating parameters.

One of the most important function of tundish is to remove the inclusions. There is an opportunity for the inclusions to be absorbed by the top slag if adequate residence time is being provided. Thus, various kinds of FCD such as dam, weir, baffle, turbulence inhibitor and gas curtain, have been installed in tundish aiming at controlling the flow pattern, so as to increase the residence time of fluids and remove the inclusions.

Plenty of modeling studies have been carried out to realize the best performance of tundish with the installation of different FCD. These studies have led to important improvements in our understanding of the various transport phenomena associated with tundish operations. A summary of the previous modeling works of flow control devices in tundish is given in Table 1. The functions of the main flow control devices (shown in Figure 1) in tundish can be summarized based on the literature study.

Table 1. Summary of modeling studies on flow control devices in tundish.

Reference	Model [1]	Code	Design			Thermal Condition	Study Focus [4]
			Strand	Fluid [2]	FCD [3]		
Miki (1999) [5]	M, P	FLUENT	1	S	W, D	Iso/Nonisothermal	V, TP, ID, IS, TKE, TDR, IRR
Palafox-Ramos (2001) [6]	N, P	-	2	S/W	TI, D	Nonisothermal	RTD, CS, TD
Vargas-Zamora (2003) [7]	N, P	-	1	W	TI, D	Nonisothermal	CIT, FP, BF, TM, TOI, TD
Rogler (2005) [8]	P	-	1	W	TI, G	Isothermal	FCD, GFR, IS, GBS, RTD, IRR
Ramos-Banderas (2006) [9]	N, P	-	1	W	TI, D, G	Isothermal	FCD, FP, V, GVF, IS,
Najera-Bastida (2007) [10]	N, P	-	2	W	TI, G	Isothermal	FCD, RTD, TD, V, FP, TKE
Zhong (2008) [11]	P	-	2	W	TI, D, W, G	Isothermal	FCD, GFR, GL, RTD
Seshadri (2012) [12]	P	-	2	W	TI, G	Isothermal	GFR, GL, IS, PM
Arcos-Gutierrez (2012) [13]	N	FLUENT	2	S	TI, G	Isothermal	V, IS, PS, GBS
Chattopadhyay (2012) [14]	N, P	FLUENT	4	S/W	TI	Nonisothermal	IRR, TC, TD, TM, FP
Singh (2012) [15]	N	FLUENT	1	S	TI, IW, B, D	Iso/Nonisothermal	CIT, TP, FP, TC
Sun (2012) [16]	N, P	-	1	S/W	TI, W, D, SR	Nonisothermal	FP, V, RTD
Merder (2013) [17]	N, P	FLUENT	2	S/W	TI	Isothermal	V, FCD, TKE, TD, RTD
He (2013) [18]	N	OpenFOAM	2	S	TI, B	Isothermal	MS, RTD, FCD, V, TKE
Hamid (2013) [19]	N, P	-	4	S/W	TI	Nonisothermal	SM, TM, RTD
Chang (2015) [20]	N, P	FLUENT	7	S /W	TI, B, G	Nonisothermal	V, FP, FCD, GP, RTD, TD
Wang (2016) [21]	N, P	-	7	S/W	TI	Nonisothermal	FCD, RTD, TD, FP, TP,
Neves (2017) [22]	N, P	CFX	2	S/W	TI, W, D, SR	Isothermal	FP, RTD
Agarwal (2019) [23]	N	FLUENT	6	S	TI	Nonisothermal	FP, TP, V, TM, RTD, TT
Mishra (2019) [24]	N	FLUENT	2	W	TI	Isothermal	RTD, V
Neumann (2020) [25]	N	OpenFOAM	2	S	TI, F	Isothermal	FP, PN, IRR
Wang (2020) [26]	N	FLUENT	2	S	W, TI, F	Isothermal	TC, FCD, IS

[1] N: numerical model; P: physical model; [2] W: water; S: steel; [3] FCD: flow control device; B: baffle; D: dam; F: Filter; IW: inclined wall; SR: stop rod; TI: turbulence inhibitor; W; weir; G: gas stirring [4] BF: buoyancy force; CIT: comparison with isothermal; CS: casting speed: flow control device; FP: flow pattern; GBS: gas bubble size; GFR: gas flow rate; GL: gas location; GVF: gas volume fraction; ID: inclusion density; IS: inclusion size; IRR: inclusion removal rate; IT: initial temperature PM: porous material; PN: particle number; PS: pore size; RTD: residence time distribution; MS: mesh size; SM: slag movement; TC: tundish configuration; TD: tracer dispersion; TDR: turbulence dissipation rate; TKE: turbulence kinetic energy; TP: temperature profile; TM: temperature measurement; TT: transition tonnage; V: velocity.

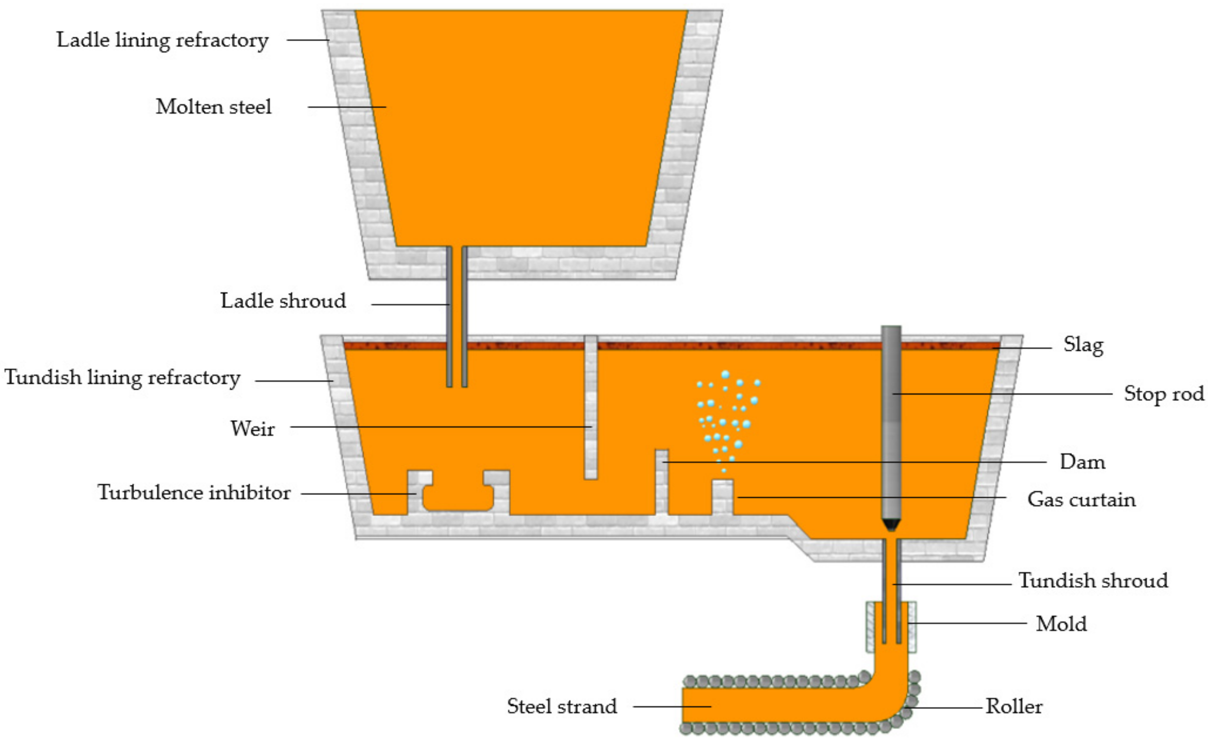

Figure 1. Schematic layout of curved continuous casting machine.

(1) Weir: It is mainly used to divide the inlet chamber and the outlet chamber. The appearance of the weir is good for controlling the turbulence in the inlet chamber, benefits the inclusion flotation and decrease the surface wave amplitude in the outlet chamber [11,16,22,26].

(2) Dam: It is mainly used to oriental the liquid flow upwards, so as to prolong the residence time of liquid steel in the tundish. The weir would produce a short circuiting, but the dam could eliminate this flow pattern [5–7,16].

(3) Turbulence inhibitor: It is widely used to prevent damage to the linings due to the high velocity of the incoming stream. The high turbulence of the incoming stream can spread throughout the tundish if the flow is not properly controlled. It may cause the disturbance of the steel/slag interface and thereby promote slag entrainment [10,14,15,17].

(4) Gas curtain: It has a strong effect on the removal of small inclusions because they are inclined to float to surface with the gas bubbles. A gas curtain, which generates a stronger recirculating flow, is helpful for the mixing. The average residence time of molten steel in the tundish prolonged and the dead volume fraction decreased when the gas curtain was applied [8,9,12,13].

From the literature study, it is clear that the numerical and physical modeling can be used to investigate the effect of FCD on fluid flow and inclusion behavior in the tundish. However, most of the abovementioned studies focused on a certain type of flow control devices. Few works attempted to have a systematic comparison of the different combinations of FCD in order to meet the increased requirement of the flexibility of tundish. For example, a combination of weir and dam is effective to cast a steel containing large inclusions. However, to cast a steel with a strict requirement of small inclusions, the introduction of gas curtain in the tundish is recommended. The gas curtain not only acts as a dam which reorients the flow, but also generates small gas bubbles which are beneficial for small inclusion removal.

The development of guidelines for the selection of FCD and the location of its installation is of paramount importance for the plant operations. Therefore, five different tundish configurations were comparatively studied in this work using both water model and CFD model. The selected configurations in the tundish can be divided into two groups: single-phase group and multiphase group. In the single-phase group, there are three tundish configurations: (i) bare tundish; (ii) weir + dam (WD); (iii) turbulence inhibitor + weir + dam (TI + WD). In the multiphase group, there are two tundish configurations: (i) weir + gas curtain (WG); (ii) turbulence inhibitor + weir + gas curtain (TI + WG). A scaled-down (1:2) water model was used to observe dye trace dispersion and measure the RTD curves. The flow patterns were evaluated and a concept design of tundish FCD was proposed based on the water model results. A CFD model was firstly validated with the experimental data, then applied to calculate the RTD curves in the prototype tundish, taking the nonisothermal conditions into account.

2. Model Description

2.1. CFD Model

CFD software STAR-CCM + V.13 (Siemens PLM software, Plano, TX, USA) was used in this study [27]. The assumptions made for the mathematical model are described below:

- The model is based on a 3D standard set of the Navier–Stokes equations.
- Nonisothermal and steady-state flow is calculated for the prototype.
- The realizable k-ε model is used to describe the turbulence.
- The motion of bubbles is simulated by solving the force balance equations.
- Boussinesq model is applied to calculate the natural convection flow.
- The heat losses of tundish prototype are considered.
- The free surface is flat and is kept at a fixed level. The slag layer is not included.

2.1.1. Transport Equation

Equations (1)–(3) are used to describe the continuous phase [28].

Continuity:

$$\frac{\partial(\rho u_j)}{\partial x_j} = 0 \tag{1}$$

Momentum:

$$\rho u_j \frac{\partial u_i}{\partial x_j} = -\frac{\partial P}{\partial x_i} + \frac{\partial}{\partial x_j}\left[(\mu + \mu_t)\left\{\frac{\partial u_i}{\partial x_j} + \frac{\partial u_j}{\partial x_i}\right\}\right] + g_i(\rho - \rho_0) \tag{2}$$

Thermal energy:

$$\rho C_p \frac{\partial T}{\partial t} + \rho C_p \frac{\partial (u_j T)}{\partial x_j} = \frac{\partial}{\partial x_j}\left[\left(k_0 + \frac{C_p \mu_t}{Pr_t}\right)\frac{\partial T}{\partial x_j}\right] + S_T \tag{3}$$

where ρ is the density; C_p is the heat capacity; μ_t is the turbulent viscosity; Pr_t is the turbulent Prandtl number (the value of 0.9). S_T represents the source term of energy equation.

Realizable k-ε model: [29]

$$\frac{\partial}{\partial t}(\rho k) + \frac{\partial}{\partial x_j}(\rho k u_j) = \frac{\partial}{\partial x_j}\left[\left(\mu + \frac{\mu_t}{\sigma_k}\right)\frac{\partial k}{\partial x_j}\right] + G_k + G_b - \rho\varepsilon - Y_M + S_k \tag{4}$$

$$\frac{\partial}{\partial t}(\rho \varepsilon) + \frac{\partial}{\partial x_j}(\rho \varepsilon u_j) = \frac{\partial}{\partial x_j}\left[\left(\mu + \frac{\mu_t}{\sigma_\varepsilon}\right)\frac{\partial \varepsilon}{\partial x_j}\right] + \rho C_1 S\varepsilon - \rho C_2 \frac{\varepsilon^2}{k + \sqrt{v\varepsilon}} + C_{1\varepsilon}\frac{\varepsilon}{k}C_3 G_b + S_\varepsilon \tag{5}$$

where k is the turbulent kinetic energy; ε is the turbulent energy dissipation rate; μ is the molecular viscosity; μ_t is the turbulent viscosity; G_k represents the generation of turbulent kinetic energy due to the mean velocity; Y_M symbolizes the contribution of the fluctuating dilatation in compressible turbulence to the overall dissipation rate; υ is the kinematic viscosity; and σ_k and σ_ε are the turbulent Prandtl numbers for k and ε, respectively.

2.1.2. Bubble Dynamics

The bubbles are considered as spherical shape, which simplifies the calculation of the force exerted by the liquid on the discrete phases significantly. The transport equation for each bubble is given as: [27]

$$m_i \frac{dv_p}{\partial t} = F_d + F_p + F_{vm} + F_g + F_l + F_{td} \tag{6}$$

where m_i and v_p denote the mass and the velocity of particle i. On the right side of Equation (6), the particle-fluid interaction forces are drag force (F_d), pressure gradient force (F_p), virtual mass forces (F_{vm}), gravitational force (F_g), lift force (F_l) and turbulent dispersion (F_{td}), respectively.

The effect of the bubble phase on the continuum is considered by incorporating the exchange of momentum as a source term in the momentum equations of the continuous phase. The drag force is defined as:

$$F_d = \frac{1}{2} C_d \rho_l A_p |v_l - v_p| \, (v_l - v_p) \tag{7}$$

where C_d is the drag coefficient of the particle, v_l and v_p denote the velocity of the liquid and the particle.

The drag force is modeled using the Schiller-Naumann model defined as: (R_e is the particle Reynolds number)

$$C_d = \begin{cases} \frac{24}{R_e}\left(1 + 0.15 R_e^{0.687}\right) & 0 < R_e \le 1000 \\ 0.44 & R_e > 1000 \end{cases} \tag{8}$$

The sum of the forces due to the pressure gradient force and gravitational forces is written as:

$$F_p + F_g = v_p \nabla P - \rho_p v_p g \tag{9}$$

The virtual mass force is defined as:

$$F_{vm} = C_{vm} \rho v_p \left(\frac{Dv}{Dt} - \frac{dv_p}{dt} \right) \tag{10}$$

where C_{vm} is the virtual mass coefficient, set to a constant value 0.5.

$$F_l = C_{ls} \frac{\rho \pi}{8} d^3 (v_p \times \omega) \tag{11}$$

where: $\omega = \nabla \times v$, the curl of the fluid velocity; C_{ls} is the lift force coefficient, set to a constant value 0.25.

A turbulent dispersion force is added to the model. The eddy velocity fluctuation is normally distributed with a zero mean and a standard deviation for the eddy velocity scale, which is calculated from the turbulence model. The root mean square (RMS) fluctuating components (v') are estimated as:

$$\sqrt{\overline{v'^2}} = \sqrt{\frac{2k}{3}} \tag{12}$$

2.1.3. Tracer Dispersion

Two passive scalar equations are solved, including (i) an instantaneous addition of the tracer at the inlet (E-curve); (ii) a continuous addition of tracers at inlet (F-curve). The passive scalar transport equations are solved at each time step once the fluid field is calculated.

$$\rho \frac{\partial \overline{C}}{\partial t} + \rho \overline{u_j} \frac{\partial \overline{C}}{\partial x_j} - \frac{\partial}{\partial x_j} \left[D_{eff} \frac{\partial \overline{C}}{\partial x_j} \right] = 0 \tag{13}$$

where D_{eff} is the effective diffusivity. The velocity field is solved obtained from a steady-state simulation and remained constant during the calculation of the passive scalar.

E-curve can be plotted based on the dimensionless outlet concentration (C-curve). Actual mean residence time is presented in Equation (14) [30,31].

$$\overline{\tau} = \frac{\int_0^\infty tC(t)dt}{\int_0^\infty C(t)dt} \tag{14}$$

The plug flow volume fraction (V_p/V), mixed flow volume fraction (V_m/V) and dead volume fraction (V_d/V) were calculated through Equations (15)–(17) [32].

Dead volume fraction,

$$V_d/V = 1 - \frac{\overline{\tau}}{\tau} \tag{15}$$

Plug flow volume fraction,

$$V_P/V = \left(\theta_{min} + \theta_{peak} \right)/2 \tag{16}$$

Mixed flow volume fraction,

$$V_m/V = 1 - V_d/V - V_p/V \tag{17}$$

where, τ is the theoretical residence time, θ_{min} is the dimensionless time of minimum concentration at the tundish outlet, θ_{peak} is the dimensionless time of peak concentration at the tundish outlet.

Another RTD expression is the cumulative distribution F-curve, which is a fraction of the liquid that has a residence time less than time (t). In this study, F-curve was analyzed to obtain an intermixing time defined as the time interval when the tracer dimensionless concentration at the outlet reaches 0.2 and 0.8.

2.1.4. Geometry, Mesh and Boundary Conditions

A single-strand tundish (51 tons) was studied in the current work. The geometric dimensions are illustrated in Figure 2.

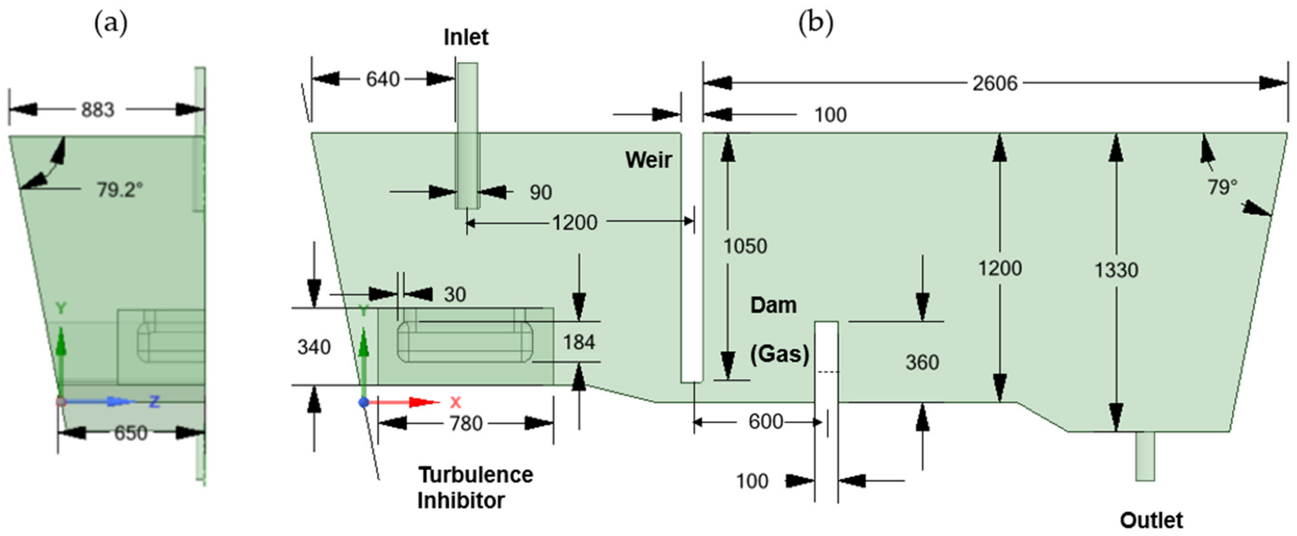

Figure 2. Dimensions of a single-strand tundish with flow control devices of dam (D), weir (W), turbulence inhibitor (TI) or gas curtain (G). (**a**) side view (unit: mm) (**b**) front view (unit: mm).

The volume mesh was generated in Star-CCM + V13 with the option of trimmer and prism layer. Three prism layers were generated next to all the walls. A base mesh size of 0.006 m was used for the simulation of tundish prototype. The average $y+$ value near the wall boundary is 3. A half tundish was simulated through its symmetry plane. The CFD model possesses a total of 3.5 million trimmer cells in the computing domain.

No-slip conditions were applied on walls for the liquid phase. A constant mass flow was used at the inlet. The outflow boundary condition was applied at the outlet. A wall function was used to provide the near-wall boundary conditions for solving the transport equations.

In the simulation of prototype tundish, the heat losses through the side and bottom walls were set to be 2.5 kW/m^2. The heat losses through the top surface were set to be 15 kW/m^2 [33].

Zero mass flux was applied at walls and top surface for solving the passive scalar equation. At t = 0–2 s the mass fraction of tracer at the inlet was set to be equal to 1. When $t > 2$ s, it was given as zero. The concentration of the tracer at the outlet was monitored from t = 0 to 2700 s and the RTD curves were obtained from the numerical calculation. A summary of input parameters and boundary conditions used for computational fluid dynamics (CFD) simulations is given in Table 2.

2.1.5. Solution Procedure

The discretized equations were solved using the semi-implicit method for the pressure-linked equations (SIMPLE) algorithm. The second-order upwind scheme was applied to calculate the convective flux in the momentum equations. The solution was considered to be converged when the residuals of all solved variables were less than 1×10^{-4}. The under-relaxation parameters for solving pressure, velocity and turbulence equations were 0.3, 0.7 and 0.8, respectively. To calculate the RTD curves in the prototype, the flow fields were first calculated in steady state. Then, the transient calculations were performed to solve the passive scalar equations.

Table 2. Input parameters and boundary conditions used for water model and CFD model.

Parameter	Water Model	CFD Model (Prototype)
Density	997 kg/m^3	7000 kg/m^3
Viscosity	0.00089 Pa·s	0.0062 Pa·s
Reference pressure	-	101,325 Pa
Heat capacity	-	760 J/kg·K
Thermal conductivity	-	41 W/m·K
Thermal expansion coefficient	-	0.000127 1/K
Liquid level	0.6 m	1.2 m
Inlet mass flow	0.0655 t/min	3.67 t/min
Inlet temperature	-	1835 K
Gas curtain flow rate	4.63 L/min	24 L/min
Wall (flow)	-	No slip
Surface (flow)	-	Free slip
Wall (heat loss)	-	2.5 kW/m^2
Surface (heat loss)	-	15 kW/m^2
Tracer inlet (E-curve)	1 ($t \leq$ 0–2 s), 0 (t > 2 s)	1 ($t \leq$ 0–2 s), 0 (t > 2 s)
Tracer inlet (F-curve)	-	1

2.2. Water Model

The water model is following the principle of geometry and dynamic similarity. Dynamic similarity should satisfy the similarity criteria of Froude. The Froude number (*Fr)* is defined in Equation (18).

$$Fr = \frac{u^2}{gL} \tag{18}$$

Thus, a relationship between water model and prototype tundish can be obtained by Froude similarity criteria, shown in Equation (20). m stands for water model and p stands for prototype tundish.

$$\left(\frac{u_m^2}{gL_m}\right)_p = \left(\frac{u_p^2}{gL_p}\right)_p \tag{19}$$

Then, liquid velocity, volumetric flow rate and time ratio between the model and the prototype are described as a function of geometric scale factor (λ), as expressed in Equations (20)–(22). The scale factor λ is 1:2. Table 2 lists the parameters of the water model, obtained by these equations.

$$\frac{u_m}{u_p} = \left(\frac{L_m}{L_p}\right)^{\frac{1}{2}} = \lambda^{0.5} \tag{20}$$

$$\frac{Q_m}{Q_p} = \frac{u_m {L_m}^2}{u_p {L_p}^2} = \lambda^{2.5} \tag{21}$$

$$\frac{\tau_m}{\tau_p} = \frac{L_m/u_m}{L_p/u_p} = \lambda^{0.5} \tag{22}$$

The water model was made of plexiglass, with a wall thickness of 10 mm. Once the water reached to the level of 600 mm and was stabilized, 200 mL salt saturated solution was used as the tracer injecting through the tundish inlet in 2 s. One conductivity probe was used to record conductivity at the outlet of the tundish. The pulse stimulus–response technique was applied to obtain RTD curves. Afterwards, the time and the concentration were transformed to a dimensionless value to compare the obtained flow characteristics. The average values of three repetitions were used for data analysis.

The schematic diagram and plexiglass model for the water model is shown in Figure 3. The objective of water model experiment was to obtain the four optimized geometrical parameters of flow control devices, including (i) distance between inlet and weir (a); (ii) distance between weir and dam/gas curtain (b); (iii) distance of tundish bottom to weir (*c*) and (iv) dam height (*d*). The single-phase orthogonal experiments were performed to optimize the weir and dam positions (*a*,*b*,*c*,*d*). The multiphase experiments, based on Taguchi orthogonal method, were performed to optimize the weir and gas curtain positions (*a*,*b*,*c*). Table 3 lists the optimized geometrical parameters based on the measured RTD curves.

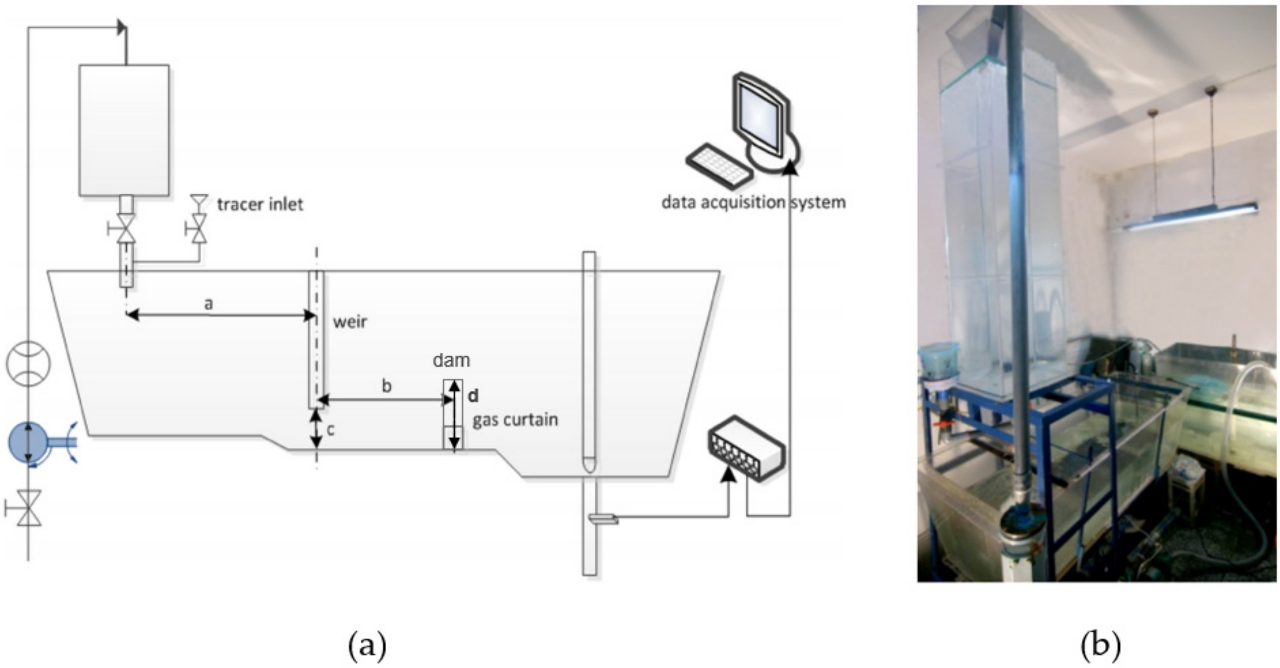

Figure 3. (**a**) Schematic diagram and (**b**) plexiglass model for water model of tundish.

Table 3. Optimized geometrical parameters of flow control devices in tundish.

Parameter	Distance between	Single-Phase (without Gas Curtain)	Multiphase (with Gas Curtain)	Prototype
a	inlet and weir	1000 mm	1400 mm	1200 mm
b	weir and dam/gas curtain	600 mm	600 mm	600 mm
c	tundish bottom to weir	100 mm	200 mm	150 mm
d	dam height	360 mm	-	360 mm

A Taguchi orthogonal array L9 was used to analyze the effects of design parameters of both single-phase and multiphase water model experiments, with the emphasis on low dead volume fraction. It can be found that the optimized geometrical parameters, based on orthogonal analysis, are different for the single-phase and multiphase systems. The proposed configuration for prototype is a compromised design, which considers a convenient plant operation, i.e., a fixed position of weir and a fixed position of dam or gas curtain. The selection of dam or gas curtain can be determined based on the process requirements. The comparative studies of tundish configurations in this work are all based on the optimized geometrical parameters, listed in Table 3 [34,35]. In addition, a bare tundish was also studied as a reference case.

In the water model experiment, the gas curtain was generated through a hollow plexiglass box connected with five gas inlets, with an inner diameter of 6 mm (Figure 4a). Three rows of blowing holes (Figure 4b) are evenly distributed on the blowing plate to generate a uniform gas curtain with small bubbles. The laser punched hole has a diameter of 0.18 mm and the vertical distances between holes are 50 mm. It was found in the water model experiments that individual hole may have a high resistance where no gas escapes.

However, due to the large number of holes that complement each other, the gas curtain was most uniformly distributed.

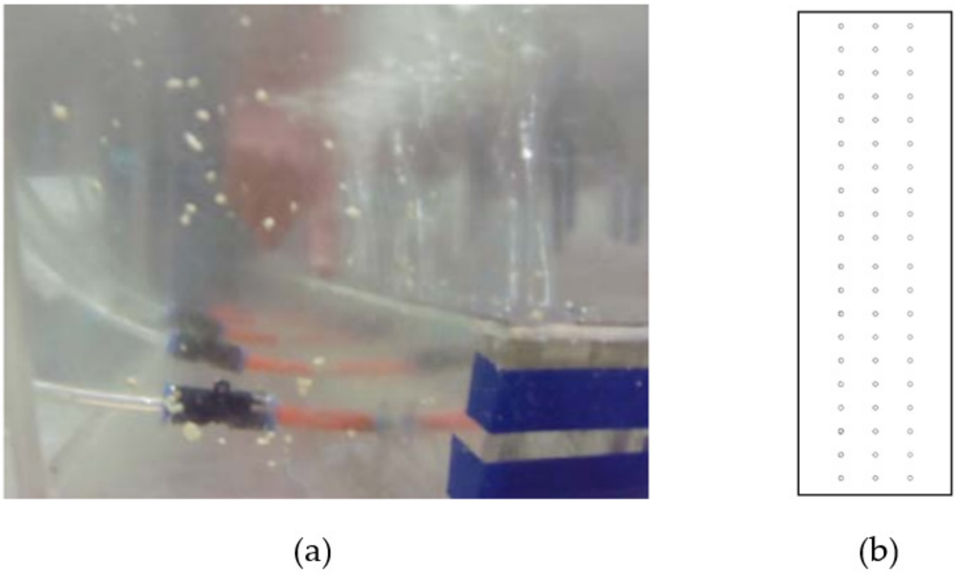

Figure 4. Gas curtain devices used in water model of tundish (**a**) side view of plexiglass box (**b**) top view of the blowing plate.

3. Results

3.1. Water Model

3.1.1. Single-Phase Experiments

Three configuration cases have been compared in the single-phase experiments in terms of tracer dispersion. They are: (i) bare tundish (bare), (ii) weir + dam (WD) and (iii) turbulence inhibitor + weir + dam (TI + WD). Figure 5 presents the tracer dispersion in water model at 10 s, 15 s and 20 s. In the bare tundish case, the inlet stream hits the bottom and spreads rapidly near the entry zone. The flow partially moves along the bottom and then reached the outlet. As shown in the photo at 20 s, the bare case leaves a rather big dead zone volume above the outlet due to the short-circuit flow. This flow pattern will negatively affect the tundish performance.

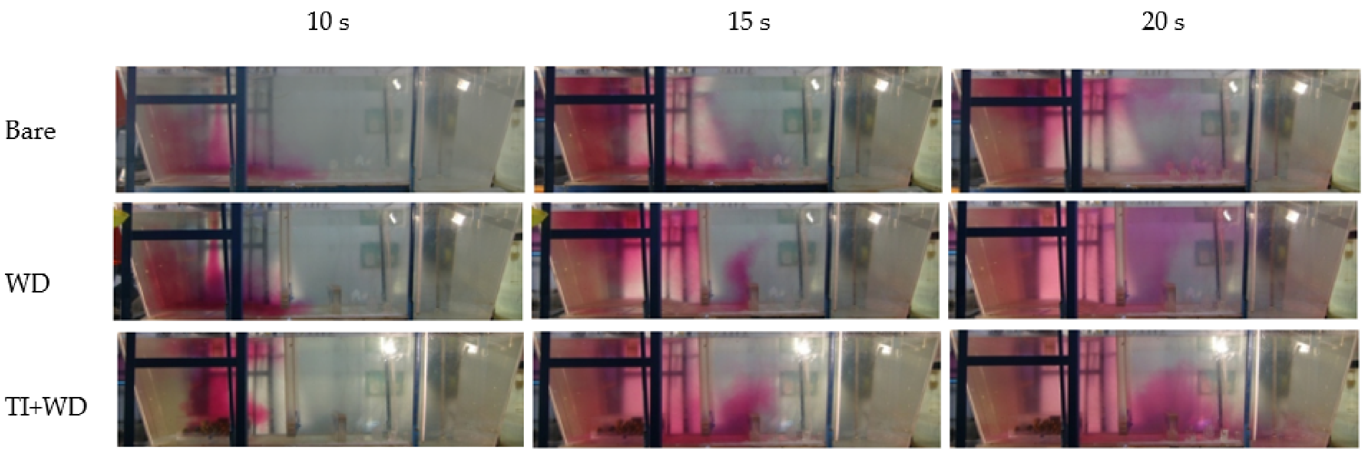

Figure 5. Tracer dispersion in cases of Bare, WD and TI + WD at 10 s, 15 s and 20 s in water experiments.

In comparison with the bare case, the installation of FCD, weir and dam, reorients the flow path. As exhibited in Figure 5 (WD case at 12 s and 20 s), the existence of the weir and dam drives the incoming stream moving upwards to the top surface, and then flowing along the side wall to the outlet. The prolonged flow path leads to a longer residence time of inclusions, leading to the increased contact possibility between inclusions and top slag layer. The inclusion removal can therefore be improved.

In terms of the TI + WD case, Figure 5 displays a different reorientation of the flow near the dam compared to the WD case. In the WD case, the high momentum entering stream once reaches the bottom after pouring, it moves horizontally along the bottom. The horizontal velocity of liquid was significantly impaired when it hits the dam. The flow was driven vertically to the top surface (Figure 5—WD at 15 s and 20 s). In the TI + WD case, the entering stream flows upwards after hitting the turbulence inhibitor (Figure 5—TI + WD at 10 s). Additionally, the flow is well mixed in the entry zone due to the circulation formed by turbulence inhibitor (Figure 5–TI + WD at 15 s). However, the bottom stream flows across the dam first, then sinks to the bottom and finally leaves the tundish through the outlet (Figure 5-TI + WD at 15 s, 20 s). The addition of turbulence inhibitor impairs the effect of dam. It shortens the flow path in the tundish.

Figure 6 shows the comparison of the RTD curves between the three single-phase cases (bare, WD and TI + WD). The bare tundish has the shortest breakthrough time, the smallest mean residence time (685 s) and the highest dead volume fraction (25%). The TI + WD case has the highest peak concentration, indicating that more tracers left the tundish quickly. This flow pattern resulted in a large dead flow volume in the tundish (19%) and a short residence time of liquid (708 s). The RTD curve of the WD case reveals a smoother shape, which indicates that the flow characteristics were improved using a weir and a dam. The result shows an increase of residence time (795 s) and a decrease of dead volume zone (14%) in the tundish when comparing with the TI + WD case. The negative effect of turbulence inhibitor shown in RTD analysis, which appears consistent with the flow observations in Figure 5.

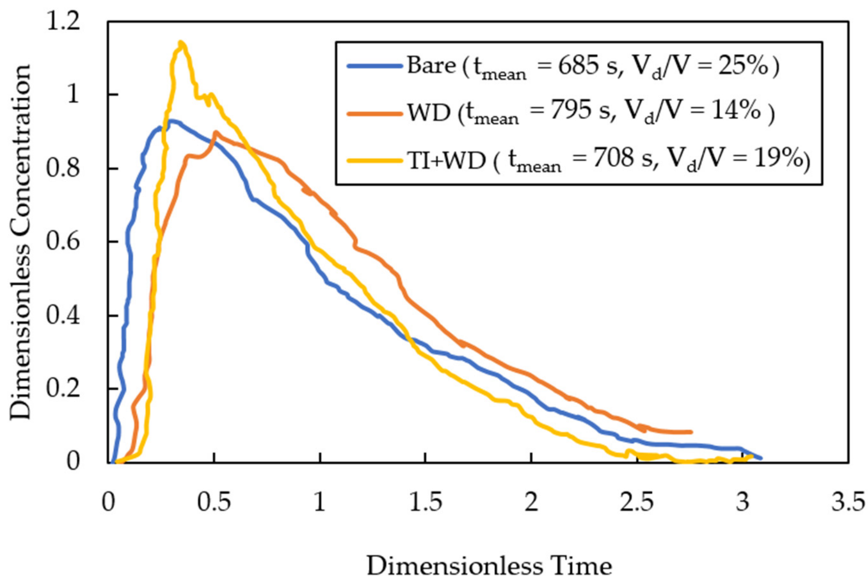

Figure 6. Comparison of measured RTD curves between three cases: bare, WD and TI + WD (theoretical residence time = 834 s).

3.1.2. Multiphase Experiments

Other than the three above mentioned single-phase cases in Section 3.1.1, another two cases with the gas curtain have also been compared in this work. They are: weir + gas (WG) case and turbulence inhibitor + weir + gas (TI + WG) case.

Figure 7 shows that the functions of the gas curtain and dam are similar. The incoming stream was driven upwards together with the floating gas bubbles (Figure 7—WG case at 15 s and 20 s). However, the impact of the gas curtain on the incoming stream is weaker than that of dam because the gas curtain is not intensive enough to effectively alter the direction of the bottom flow with an upward momentum. When it is placed with turbulence inhibitor, the velocity of bottom stream velocity declines. Thus, the gas curtain can better drive the flow to the water surface.

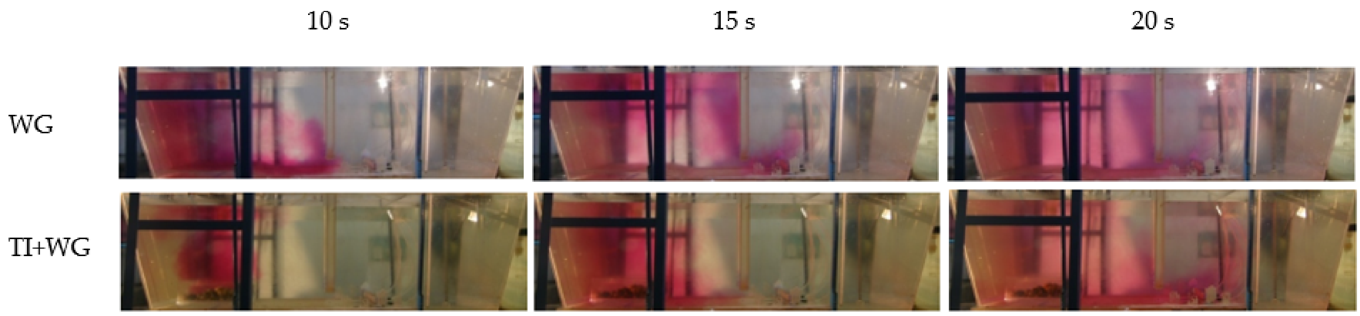

Figure 7. Tracer dispersion in cases of WG and TI + WG at 10 s, 15 s and 20 s in water experiments.

Figure 8 shows the comparison of RTD curves between the two multiphase cases (WG and TI + WG). The TI + WG case has a longer mean residence time (796 s) and a lower dead volume fraction (9%) when comparing with the WG case. The RTD curve of the TI + WG case reveals the prolonged breakthrough and peak concentration time, indicating an improved performance in inclusion removal. The positive effect of the turbulence inhibitor is observed in the RTD analysis, which appears consistent with the flow observations in Figure 7.

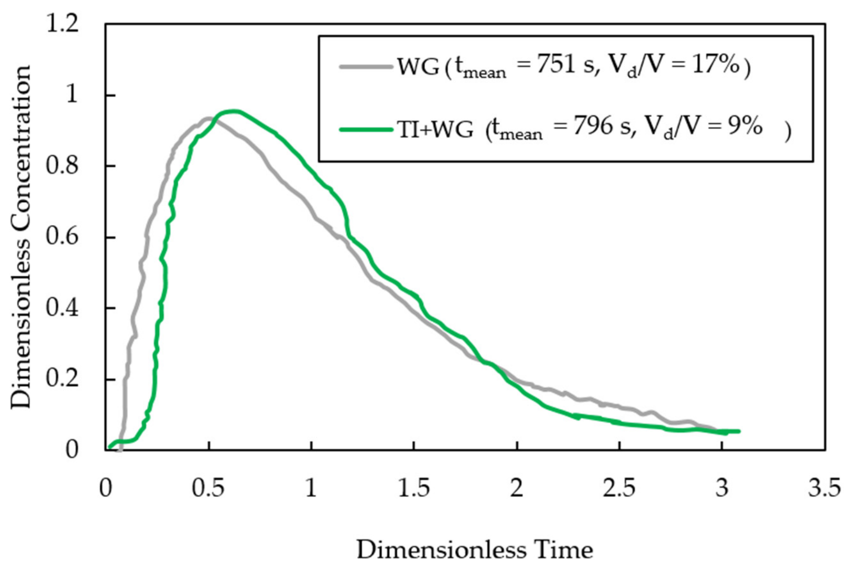

Figure 8. Comparison of measured RTD curves between two cases: WG and TI + WG (Theoretical residence time = 834 s).

3.2. CFD Model of Prototype Tundish

3.2.1. Validation of CFD Model

Best practice guidelines (BPG) are important to ensure the accuracy and credibility of CFD predictions. The CFD model development in this work followed with the general guidelines from the references [36–38]. Figure 9 displays the local CFD mesh in the computing domain of the tundish (near the turbulence inhibitor and inlet region, zoom-in view). The validation and verification of the CFD model including mesh dependency and comparison with the experimental data can be found in previous works [39,40].

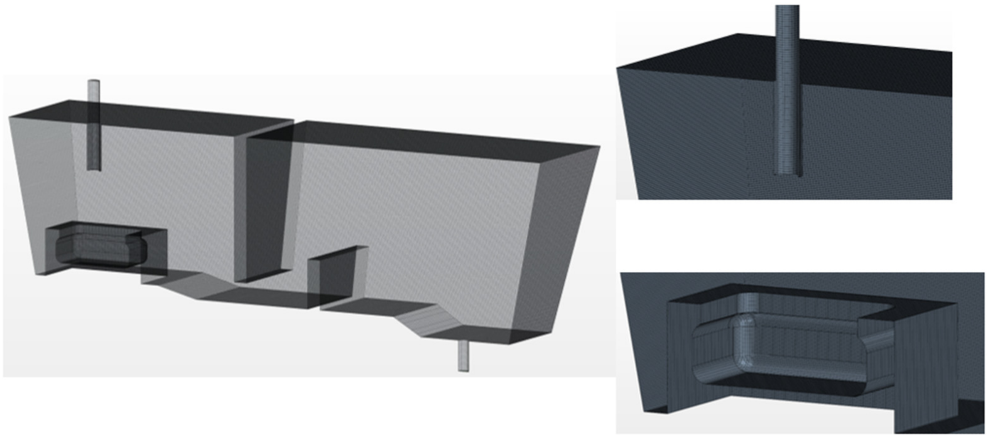

Figure 9. Computational domain and local CFD mesh of single-strand tundish (zoom-in view).

Figure 10 displays the simulated RTD plots against the measured RTD plots from the water model experiment of two cases: TI + WD (single-phase) and WG (multiphase). The detailed input data for the CFD model can be found in [34]. A good matching of the breakthrough time is observed, compared the numeric results to the physical modeling results. The predicted peak values agreed well with the water experiment. The slopes of the E-curves after the peak were close to each other. Thus, the overall comparison between the simulation and the experiment is satisfactorily close.

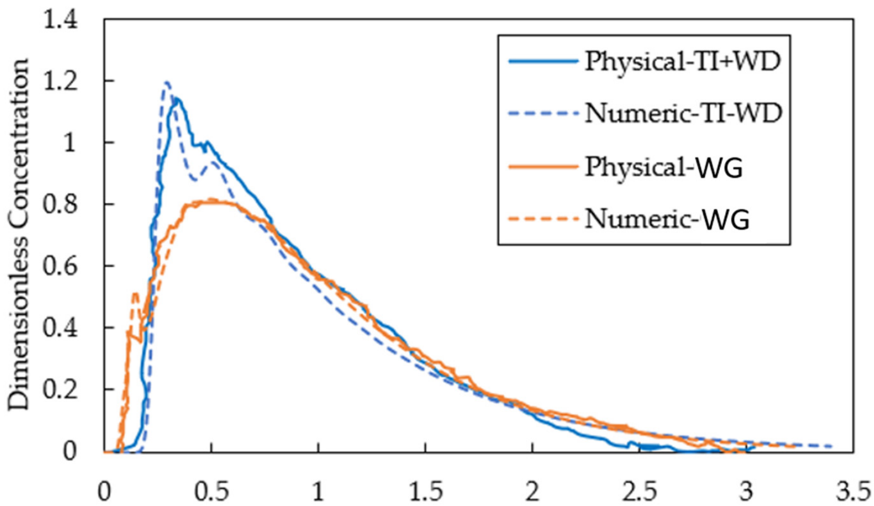

Figure 10. RTD curves of physical modeling and numerical modeling results in single-phase case TI + WD and multiphase case WG.

3.2.2. Single-Phase Simulations

Three single-phase cases were calculated for the prototype tundish with configurations: (i) bare tundish, (ii) weir + dam (WD) and (iii) turbulence inhibitor + weir + dam (TI + WD). Figure 11 shows the predicted flow pattern and temperature distributions on the symmetry plane after pouring the molten steel from ladle. For the bare tundish and WD cases, the entering liquid hits the bottom and spreads rapidly. The stream moves along the left sidewall, then flows back to the inlet jet. It forms a counter flow near the inlet region. In the outlet chamber, a clockwise circulation loop is observed in the WD and TI + WD cases (Figure 11b,c) resulting from the effect of thermal buoyancy. When the tundish was equipped with a turbulence inhibitor, the entering flow reoriented towards the top surface and formed circulation loops in the inlet chamber.

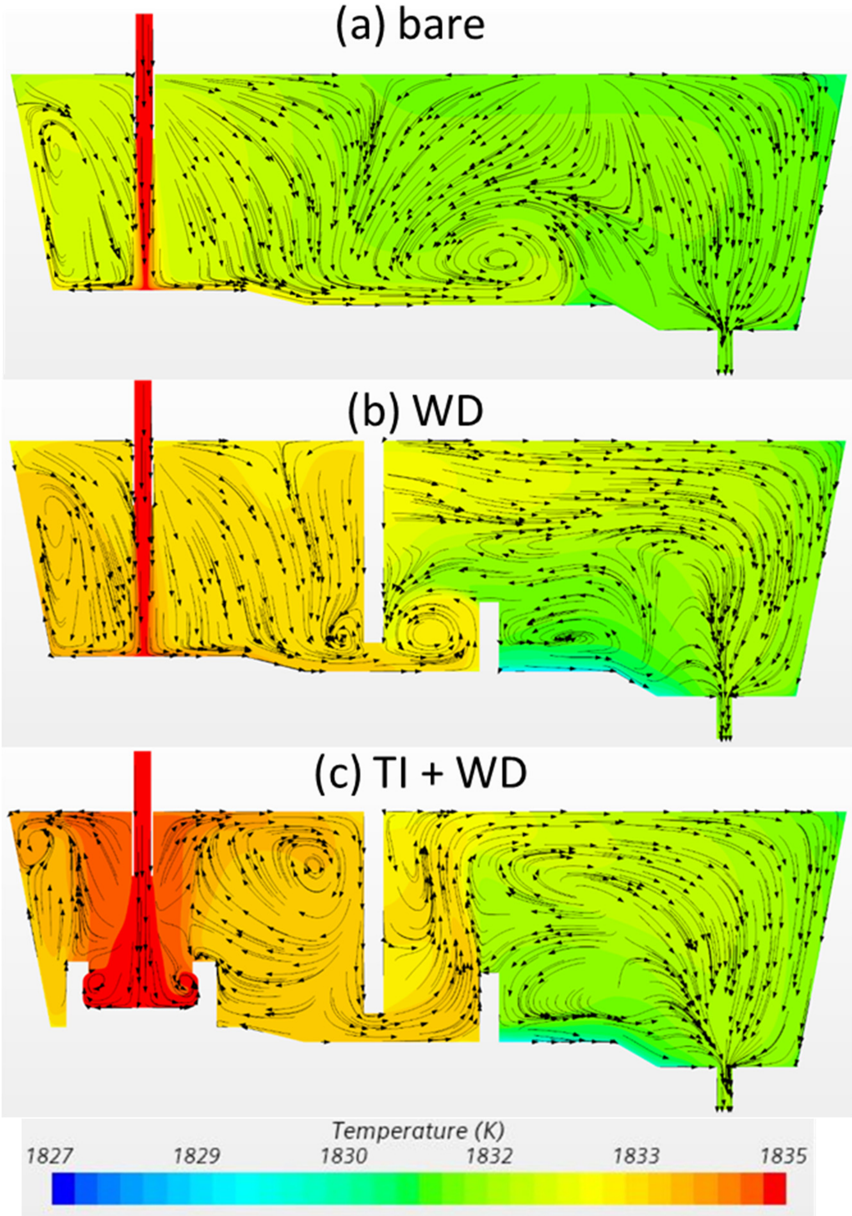

Figure 11. Fluid flow and temperature distributions in tundish for three single-phase cases with different configurations: (**a**) bare; (**b**) WD; (**c**) TI + WD.

As shown in Figure 11, the TI + WD case has the highest temperature in the inlet chamber, indicating a good mixing owing to the presence of turbulence inhibitor. On the contrary, the bare tundish has the lowest temperature in the inlet region which means a poor mixing. Thermal buoyancy has a significant effect on the temperature distributions in the outlet chamber. In Figure 11b,c, the lowest temperature is located near the bottom behind the dam. A stronger temperature gradient is observed in the outlet chamber of the WD case (Figure 11b) in comparison with the TI + WD case. This means that the turbulence inhibitor creates a more uniform temperature in the inlet chamber which decreases the effect of the thermal buoyancy in the outlet chamber (Figure 11c).

Figure 12 and Table 4 display the calculated E-curve, F-curve and RTD analysis for the three single-phase cases. In Figure 12a, the E-curve of bare tundish has the highest peak value and the shortest breakthrough time (73 s). For the tundish with the weir and dam, the peak value of the E-curve decreases and the breakthrough time increases (108 s). Case TI + WD has the lowest peak value and longest breakthrough time (179 s). The theoretical residence time are not the same for the three cases since the volume of tundish changes with the different configuration. The dead volume fraction of cases bare, WD and TI + WD are 20%, 15% and 7%, respectively. The presence of a turbulence inhibitor shows a positive effect on the tundish performance in the prototype tundish.

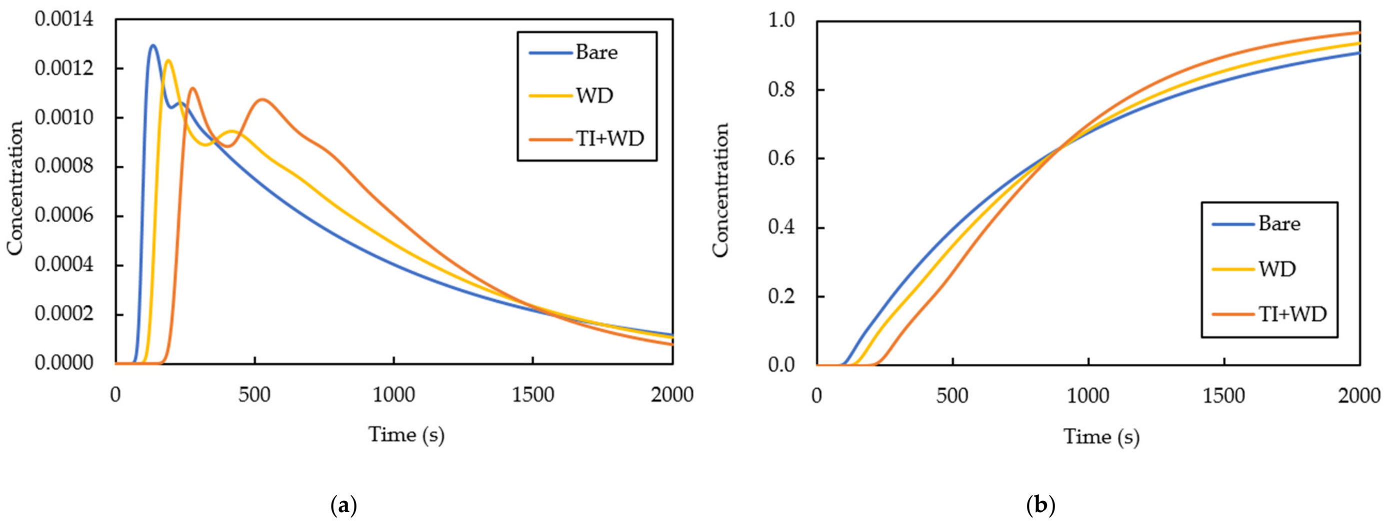

Figure 12. (**a**) E-curve and (**b**) F-curve for single-phase tundish configurations: bare, WD, and TI + WD.

Table 4. Computational RTD parameters and the volume fraction of flow for Case bare, WD and TI + WD.

Case	$t_{theoretical}$ (s)	t_{mean} (s)	t_{min} (s)	t_{max} (s)	$t_{0.2}$ (s)	$t_{0.8}$ (s)	t_{mix} (s)	V_d/V (%)	V_p/V (%)	V_m/V (%)
Bare	873	702	73	136	273	1387	1114	20	8	72
WD	848	719	108	191	336	1293	957	15	13	72
TI + WD	834	774	179	279	426	1199	773	7	21	71

This is contrary to the results from the water model experiment (Figure 6). One explanation is the effect of thermal buoyancy. In the isothermal water model experiment, the upward flow driven by dam is mainly determined by the horizontal momentum of fluids hitting the dam. The turbulence inhibitor leads to a change of flow direction in the inlet chamber, which decreases the horizontal momentum of fluids along the bottom underneath the weir. Thus, the upward momentum driven by dam decreases which shortens the residence time of fluids. However, in the prototype tundish furnished with the weir and dam, the bottom fluids underneath the weir have a relative lower temperature considering the nonisothermal conditions. The dam reorients the stream flowing upwards, but the cold stream flows downwards just after it runs over the dam [33]. With the installation of the turbulence inhibitor, the strong mixing in the inlet chamber leads to an increase of the temperature of bottom fluids under the weir, thus preventing a short-circuit flow caused by thermal buoyancy and prolong the residence time of fluids in the tundish.

An F-curve was applied to study the intermixing length of casting product during the ladle changeover operation [41]. Figure 12b shows the CFD modeling results of the F-curves in the prototype tundish. The model assumes that an intermixing zone exists between the value 0.2 and 0.8 of the dimensionless concentration of the tracer. The slope of the F-curves changes with the different tundish configurations (bare, WD and TI + WD). The predicted intermixing time for bare, WD and TI + WD is 1114 s, 957 s and 773 s, respectively. The tundish equipped with turbulence inhibitor, weir and dam generates the shortest intermixing time.

3.2.3. Multiphase Simulations

Two multiphase cases were calculated for the prototype tundish with configurations: (i) weir + gas curtain (WG), (ii) turbulence inhibitor + weir + gas curtain (TI+WG).

Figure 13 shows the predicted flow pattern and temperature distributions on the symmetry plane. The flow pattern in the inlet chamber is similar to the single-phase cases, shown in Figure 11. In the outlet chamber, the presence of gas curtain leads to an increased steel velocity. Two backflows are observed at each side of the gas plume. One flows towards the weir, while the other proceeds opposite, along the top surface towards to the upper-right corner. A strong clockwise recirculation loop is observed in the right part of the outlet chamber. The gas curtain redirects the downstream flow after the weir, which has a similar function as the dam. In the outlet chamber, the difference of flow patterns of case WG and case TI+WG is mainly caused by the effects of thermal buoyancy.

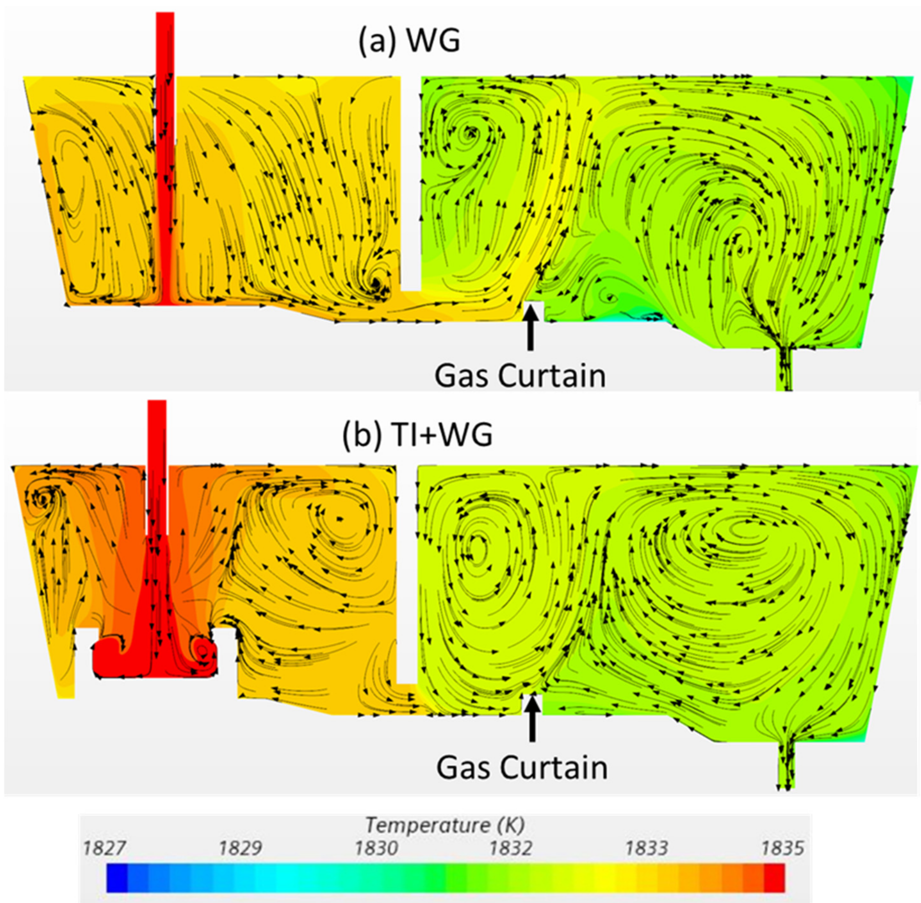

Figure 13. Fluid flow and temperature distributions in tundish for two multiphase cases with different configurations: (**a**) WG; (**b**) TI + WG.

As temperature distributions shown in Figure 13, TI+WG case has a higher temperature in the inlet chamber owing to the good mixing caused by the turbulence inhibitor. The temperature stratification in the outlet chamber tends to be alleviated due to the strong stirring capacities of the gas curtain in comparison with the single-phase cases (Figure 11). The temperature is more evenly distributed in the tundish for the TI+WG case.

Figure 14 and Table 5 give the calculated E-curve, F-curve and RTD analysis for the two multiphase cases. E-curve of the TI + WG case has a higher peak value and a longer breakthrough time (128 s). For the WG case, the breakthrough time is 66 s. In comparison with the WG case, the presence of turbulence inhibitor decreases the dead volume fraction from 10% to 7% and increases the plug flow volume fraction from 8% to 15%, which creates a favorite flow condition for the inclusion removal [42]. Figure 14b shows the CFD modeling results of the F-curves in the prototype tundish for the cases WG and TI + WG. The slope of the two F-curves are quite similar. The predicted intermixing time are 874 s and

788 s, for the cases WG and TI+WG respectively. The tundish equipped with turbulence inhibitor, weir and gas curtain generates a shorter intermixing time.

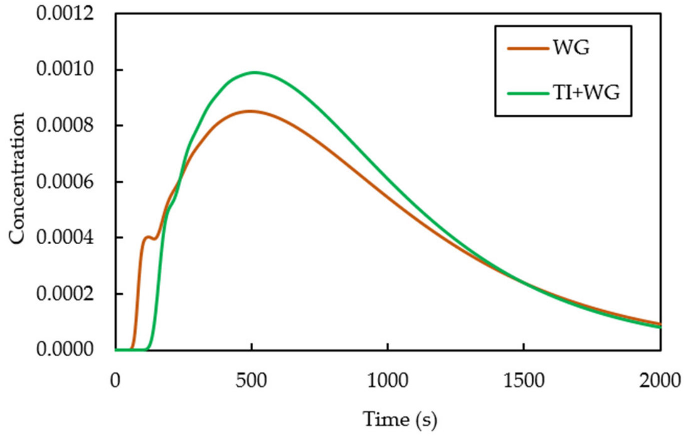

(**a**)

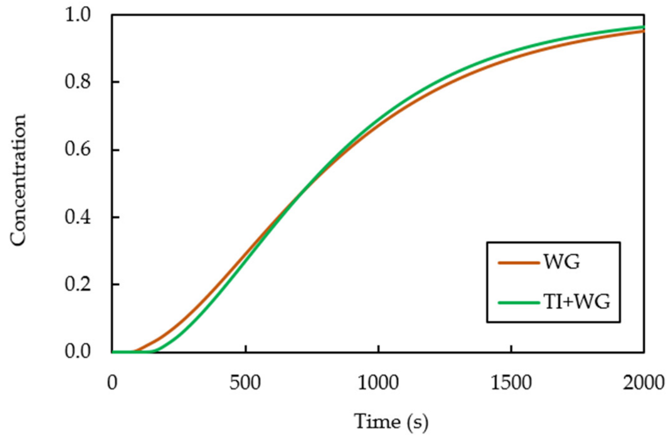

(**b**)

Figure 14. (**a**) E-curve and (**b**) F-curve for multiphase tundish configurations: WG and TI + WG.

Table 5. Computational RTD parameters and the volume fraction of flow for the cases WG and TI + WG.

Case	$t_{theoretical}$ (s)	t_{mean} (s)	t_{min} (s)	t_{max} (s)	$t_{0.2}$ (s)	$t_{0.8}$ (s)	t_{mix} (s)	V_d/V (%)	V_p/V (%)	V_m/V (%)
WG	852	768	66	496	398	1272	874	10	8	82
TI+WG	838	780	128	513	428	1216	788	7	15	78

4. Conclusions

Water modeling and CFD modeling were performed to investigate the effect of weir, dam, turbulence inhibitor and gas curtain on the performance of tundish. The main findings from the study are summarized as below:

- In the single-phase water experiments, bare tundish has the highest dead volume fraction (25%). The configuration of TI + WD and WD resulted in a dead volume fraction 19% and 14%, respectively. The result indicates that the presence of the turbulence inhibitor can impair the effect of dam, which leads to an increase of the dead volume fraction.
- In the multiphase water experiments, the configuration of TI + WG and WG resulted in a dead volume fraction of 9% and 17%, respectively. In comparison with WG case, the RTD curve of TI + WG case reveals the prolonged breakthrough time and peak-concentration time, indicating an improved performance in inclusion removal.
- The overall comparison of the RTD curves between the CFD simulation and the water experiment is satisfactorily close for both single-phase and multiphase flow. In the single-phase CFD prototype modeling, the dead volume fraction of cases Bare, WD and TI + WD is 20%, 15% and 7%, respectively. The predicted intermixing time for bare, WD and TI + WD is 1114 s, 957 s and 773 s, respectively. The tundish equipped with turbulence inhibitor, weir and dam generates the lowest dead volume fraction and the shortest intermixing time.
- In the multiphase CFD prototype modeling, in comparison with the WG case, the presence of turbulence inhibitor (TI + WG) decreases the dead volume fraction from 10% to 7% and increases the plug flow volume fraction from 8% to 15%. The predicted intermixing time are 874 s and 788 s, for the cases WG and TI + WG respectively.
- A compromised design of prototype tundish was proposed considering a convenient plant operation. The four geometrical parameters of flow control devices are (i) dis-

tance between inlet and weir (*a*), 1200 mm; (ii) distance between weir and dam/gas curtain (*b*), 600 mm; (iii) distance of tundish bottom to weir (*c*), 150 mm and (iv) dam height (*d*), 360 mm. The positions of flow control devices can be kept unchanged during the plant operations. The dam can be replaced by the gas curtain depending on the product requirements.

Author Contributions: Investigation, D.-Y.S. and D.C.; Methodology, D.-Y.S. and D.C.; Writing—Original Draft Preparation, D.-Y.S.; Writing—Review and Editing, D.-Y.S.; Validation, D.C.; Project Administration and Funding Acquisition, D.-Y.S. All authors have read and agreed to the published version of the manuscript.

Funding: This paper was supported by Swedish Foundation for Strategic Research (SSF)- Strategic Mobility Program (2019).

Institutional Review Board Statement: Not applicable.

Informed Consent Statement: Not applicable.

Data Availability Statement: The data presented in this study are available on request from the corresponding author.

Acknowledgments: The work is supported by Swedish Foundation for Strategic Research (SSF)—Strategic Mobility Program (2019).

Conflicts of Interest: The authors declare no conflict of interest.

Nomenclature

A_p	Area of Particle	S_F	Source term
$C(t)$	Tracer concentration at time t	S_T	Source term of energy equation
C_p	Heat capacity	t	Time
C_d	Drag coefficient of particle	u	Velocity
C_{vm}	Virtual mass coefficient	v	Kinematic viscosity
C_{ls}	Lift force coefficient	v_l	The velocity of liquid
D_{eff}	Effective diffusivity	v_p	The velocity of particle
$E(t)$	Residence-time distribution	v'	Fluctuating velocity component
$E(\theta)$	Dimensionless residence-time distribution	v_r	Relative velocity between steel and gas
F_d	Drag force	V	Volume of tundish
F_p	Pressure gradient force	V_p	Plug flow volume
F_{vm}	Virtual mass forces	V_m	Mixed flow volume
F_g	Gravitational force	V_d	Dead zone volume
F_l	Lift force	x_j	Cartesian coordinates
F_{td}	Turbulent dispersion	β_p	volumetric thermal expansion of liquid steel
g	Gravity	ε	Turbulent energy dissipation rate
G_k	Generation term of turbulent kinetic energy	μ	Molecular viscosity
H	Bath height	μ_t	turbulent viscosity
k	Turbulent kinetic energy	ρ	Density
L	Length	τ	Theoretical residence time
m_i	Mass	θ	Dimensionless time
N_b	Number of bubbles	θ_{min}	breakthrough time
P	Pressure	θ_{peak}	Peak dimensionless time
Pr	Turbulent Prandtl number	σ_k	turbulent Prandtl numbers for k
Q	Volumetric flow rate	σ_ε	turbulent Prandtl numbers for ε
r_b	Bubble radius	Y_M	Dilatation dissipation term
Re	Reynolds number	ω	The curl of the fluid velocity
Re_b	Reynolds number for bubbles		

References

1. Heaslip, L.J.; McLean, A.; Harris, D.J.; Young, J.D. Tundish Metallurgy and Water Modeling. In *Continuous Casting*, 1st ed.; ISS: Warrendale, PA, USA, 1983; pp. 93–112.
2. Szekely, J.; Ilegbusi, O. *The Physical and Mathematical Modeling of Tundish Operations*; Springer-Verlag: New York, NY, USA, 1989.
3. Mazumdar, D.; Guthrie, R.I.L. The physical and mathematical modelling of continuous casting tundish systems. *ISIJ Int.* **1999**, *39*, 524–547. [CrossRef]
4. Chattopadhyay, K.; Isac, M.; Guthrie, R.I.L. Physical and mathematical modelling of steelmaking tundish operations: A review of the last decade (1999–2009). *ISIJ Int.* **2010**, *50*, 331–348. [CrossRef]
5. Miki, Y.; Thomas, B.G. Modeling of inclusion removal in a tundish. *Metall. Mater. Trans. B* **1999**, *30*, 639–654. [CrossRef]
6. Palafox-Ramos, J.; de Barreto, J.J.; López-Ramírez, S.; Morales, R.D. Melt flow optimisation using turbulence inhibitors in large volume tundishes. *Ironmak. Steelmak.* **2001**, *28*, 101–109. [CrossRef]
7. Vargas-Zamora, A.; Morales, R.D.; Díaz-Cruz, M.; Palafox-Ramos, J.; Demedices, G. Heat and mass transfer of a convective-stratified flow in a trough type tundish. *Int. J. Heat Mass Transf.* **2003**, *46*, 3029–3039. [CrossRef]
8. Rogler, J.P.; Heaslip, L.J.; Mehrvar, M. Physical modelling of inclusion removal in a tundish by gas bubbling. *Can. Metall. Q.* **2005**, *44*, 357–368. [CrossRef]
9. Ramos-Banderas, A.; Morales, R.D.; de Barreto, J.J.; Solorio-Diaz, G. Modelling study of inclusions removal by bubble flotation in the tundish. *Steel Res. Int.* **2006**, *77*, 325–335. [CrossRef]
10. Nájera-Bastida, A.; Garcia-Demedices, L.; Ramirez-Lopez, P.; Torres-Alonso, E.; Morales, R.D. Dissipation of turbulent kinetic energy in a tundish by inhibitors with different designs. *Steel Res. Int.* **2007**, *78*, 318–326. [CrossRef]
11. Zhong, L.C.; Li, L.Y.; Wang, B.; Zhang, L.; Zhu, L.X.; Zhang, Q.F. Fluid flow behaviour in slab continuous casting tundish with different configurations of gas bubbling curtain. *Ironmak. Steelmak.* **2008**, *35*, 436–440. [CrossRef]
12. Seshadri, V.; da Silva, C.A.; da Silva, I.A.; da Júnior, E.S.A. A physical modelling study of inclusion removal in tundish using inert gas curtain. *Tecnol. Metal. Mater. Min.* **2012**, *9*, 22–29. [CrossRef]
13. Arcos-Gutierrez, H.; de Barreto, J.J.; Garcia-Hernandez, S.; Ramos-Banderas, A. Mathematical analysis of inclusion removal from liquid steel by gas bubbling in a casting tundish. *J. Appl. Math.* **2012**, *2012*, 534275. [CrossRef]
14. Chattopadhyay, K.; Isac, M.; Guthrie, R.I.L. Modelling of non-isothermal melt flows in a four strand delta shaped billet caster tundish validated by water model experiments. *ISIJ Int.* **2012**, *52*, 2026–2035. [CrossRef]
15. Singh, V.; Ajmani, S.K.; Pal, A.R.; Singh, S.K.; Denys, M.B. Single strand continuous caster tundish furniture comparison for optimal performance. *Ironmak. Steelmak.* **2012**, *39*, 171–179. [CrossRef]
16. Sun, H.; Yan, B.; Zhang, J. *Effect of Thermal Buoyancy Force on the Flow, Temperature Distribution and Residence Time Distribution of Molten Steel in the Slab Casting Tundish*; CFD Modeling and Simulation in Materials Processing; John Wiley & Sons: Maitland, FL, USA, 2012; pp. 327–334.
17. Merder, T. The influence of the shape of turbulence inhibitors on the hydrodynamic conditions occuring in a tundish. *Arch. Metall. Mater.* **2013**, *58*, 1111–1117. [CrossRef]
18. He, Z.; Zhou, K.; Liu, S.; Xiong, W.; Li, B. Numerical modeling of the fluid flow in continuous casting tundish with different control devices. *Abstr. Appl. Anal.* **2013**, *2013*, 984894. [CrossRef]
19. Hamid, A.K.; Isac, M.; Guthrie, R. Effect of an optimized impact pad on molten steel quality in a 4-strand delta-shaped tundish. In Proceedings of the AISTech—Iron and Steel Technology Conference, Pittsburgh, PA, USA, 6–9 May 2013; Volume 2, pp. 2143–2154.
20. Chang, S.; Zhong, L.; Zou, Z. Simulation of flow and heat fields in a seven-strand tundish with gas curtain for molten steel continuous-casting. *ISIJ Int.* **2015**, *55*, 837–844. [CrossRef]
21. Wang, M.; Zhang, C.-j.; Li, R. Uniformity evaluation and optimization of fluid flow characteristics in a seven-strand tundish. *Int. J. Miner. Metall. Mater.* **2016**, *23*, 137–145. [CrossRef]
22. Neves, L.; Tavares, R.P. Analysis of the mathematical model of the gas bubbling curtain injection on the bottom and the walls of a continuous casting tundish. *Ironmak. Steelmak.* **2017**, *44*, 559–567. [CrossRef]
23. Agarwal, R.; Singh, M.K.; Kumar, R.B.; Ghosh, B.; Pathak, S. Extensive analysis of multi strand billet caster tundish using numerical technique. *World J. Mech.* **2019**, *9*, 29–51. [CrossRef]
24. Mishra, R.; Mazumdar, D. Numerical analysis of turbulence inhibitor toward inclusion separation efficiency in tundish. *Trans. Indian Inst. Met.* **2019**, *72*, 889–898. [CrossRef]
25. Neumann, S.; Asad, A.; Schwarze, R. Numerical simulation of an industrial-scale prototypical steel melt tundish considering flow control and cleaning strategies. *Adv. Eng. Mater.* **2020**, *22*, 1900658. [CrossRef]
26. Wang, Q.; Zhang, C.-j.; Li, R. CFD investigation of effect of multi-hole ceramic filter on inclusion removal in a two-strand tundish. *Metall. Mater. Trans. B* **2020**, *51*, 276–292. [CrossRef]
27. Siemens, P.L.M. *STAR-CCM + User Guide Version 13.04*; Siemens PLM Software Inc: Munich, Germany, 2019.
28. Patankar, S.V. *Numerical Heat Transfer and Fluid Flow*; Hemisphere Publishing Corporation: New York, NY, USA, 1980.
29. Shih, T.H.; Liou, W.W.; Shabbir, A.; Yang, Z.; Zhu, J. A New k-ε eddy viscosity model for high reynolds number turbulent flows-model development and validation. *Comput. Fluids* **1994**, *24*, 227–238. [CrossRef]
30. Levenspiel, O. *Chemical Reaction Engineering*, 3rd ed.; Wiley: New York, NY, USA, 1999; pp. 283–335.
31. Sheng, D.-Y.; Zou, Z. Application of tanks-in-series model to characterize non-ideal flow regimes in continuous casting tundish. *Metals* **2021**, *11*, 208. [CrossRef]

32. Jha, P.K.; Dash, S.K. Effect of outlet positions and various turbulence models on mixing in a single and multi strand tundish. *Int. J. Numer. Methods Heat Fluid Flow* **2002**, *12*, 560–584. [CrossRef]
33. Sheng, D.-Y.; Jönsson, P.G. Effect of thermal buoyancy on fluid flow and residence-time distribution in a single-strand tundish. In *Materials*; 2021; Volume 14. [CrossRef]
34. Chen, D.F.; Xie, X.; Long, M.J.; Zhang, M.; Zhang, L.L.; Liao, Q. Hydraulics and mathematics simulation on the weir and gas curtain in tundish of ultrathick slab continuous casting. *Metall. Mater. Trans. B* **2014**, *45*, 392–398. [CrossRef]
35. Zhang, M. Simulation on Fluid Flow in Tundish with Different Flow Control Devices. Master's Thesis, The Chongqing University, Chongqing, China, November 2011.
36. Casey, M.; Wintergerste, T.; European Research Community on Flow, Turbulence and Combustion. *ERCOFTAC Best Practice Guidelines: ERCOFTAC Special Interest Group on "Quality and Trust in Industrial CFD"*; ERCOFTAC: Bushey, UK, 2000.
37. Odenthal, H.J.; Javurek, M.; Kirschen, M. CFD benchmark for a single strand tundish (Part I). *Steel Res. Int.* **2009**, *80*, 264–274. [CrossRef]
38. Odenthal, H.J.; Javurek, M.; Kirschen, M.; Vogl, N. CFD benchmark for a single strand tundish (Part II). *Steel Res. Int.* **2010**, *81*, 529–541. [CrossRef]
39. Sheng, D.Y. Mathematical modelling of multiphase flow and inclusion behavior in a single-strand tundish. *Metals* **2020**, *10*, 1213. [CrossRef]
40. Sheng, D.Y.; Yue, Q. Modeling of fluid flow and residence-time distribution in a five-strand tundish. *Metals* **2020**, *10*, 1084. [CrossRef]
41. Michalek, K.; Gryc, K.; Tkadleckova, M.; Bocek, D. Model study of tundish steel intermixing and operational verification. *Arch. Metall. Mater.* **2012**, *57*, 291–296. [CrossRef]
42. Sheng, D.-Y. Design optimization of a single-strand tundish based on cfd-taguchi-grey relational analysis combined method. *Metals* **2020**, *10*, 1539. [CrossRef]